Tapping into a phospholipid-LRH-1 axis yields a powerful anti-inflammatory agent with *in vivo* activity against colitis

Suzanne G. Mays[1a], Emma H. D'Agostino[1a], Autumn R. Flynn[2], Xiangsheng Huang[3], Guohui Wang[3], Xu Liu[1], Elizabeth J. Millings[1,4], C. Denise Okafor[1], Anamika Patel[1], M. Lee Cato[1], Jeffery L. Cornelison[2], Dianna Melchers[5], Rene Houtman[5], David D. Moore[3], John W. Calvert[4], Nathan T. Jui[2*], and Eric A. Ortlund[1*]

Departments of [1]Biochemistry, [2]Chemistry, and [3]Surgery, Emory University, Atlanta, GA 30322; [4]Department of Molecular and Cell Biology, Baylor College of Medicine, Houston, TX, [5]PamGene International B.V., 5211 HH Den Bosch, the Netherlands

[a]These authors contributed equally

[*]To whom correspondence should be addressed:

Eric A. Ortlund
Department of Biochemistry
Emory University
1510 Clifton Rd., G235
Atlanta, GA 30322
eortlun@emory.edu

Nathan T. Jui
Department of Chemistry
Emory University
1515 Dickey Drive, 456
Atlanta, GA 30322
nathan.jui@emory.edu

Running title: Phospholipid mimetics as LRH-1 agonists

Abstract

As ligands for nuclear hormone receptors (NRs), phosphatidylcholines are powerful signaling molecules. Here, we demonstrate that mimicking phosphatidylcholine-NR interactions is a robust strategy for improving agonists of liver receptor homolog-1 (LRH-1), a promising therapeutic target for diabetes and colitis. Conventional LRH-1 modulators only occupy part of the binding pocket, leaving vacant a region important for phosphatidylcholine binding and allostery. Therefore, we constructed a set of hybrid molecules that incorporate elements of natural phosphatidylcholines into the scaffold of a synthetic LRH-1 agonist. The phosphatidylcholine-mimicking group increases LRH-1 binding affinity and transcriptional activity via formation of productive interactions with residues that coordinate the phosphatidylcholine headgroup. In organoid and *in vivo* models of colitis, the best new agonist upregulates LRH-1-controlled anti-inflammatory genes and significantly improves colonic histopathology and disease-related weight loss. This is the first evidence of *in vivo* efficacy for an LRH-1 modulator in colitis, a leap forward in agonist development.

Introduction

Phospholipids (PLs) comprise a diverse family of amphipathic lipids characterized by a phosphate-containing headgroup and two fatty acyl tails of varied lengths and saturation states. PLs play many roles in physiology, including forming lipid bilayers, signaling for apoptosis, and activating G-protein coupled receptors.[1-3] PLs are labile and are synthesized and catabolized in response to stimuli such as fed or fasting states, stress, and circadian rhythms,[4-6] yielding metabolites that perform specialized functions.

Phosphatidylcholines (PCs) are a subtype of PL that are the most abundant component of eukaryotic cellular membranes and are vital for maintaining membrane integrity and curvature.[7] In

addition to these structural roles, PCs are important cell signaling mediators. Catabolism of PCs produces bioactive molecules such as arachidonic acid and diacylglycerol.[8] PC catabolism also generates labile methyl groups used for DNA methylation and for synthesis of molecules such as nucleotides and amino acids.[9] Catabolism of PCs is not required for bioactivity: certain intact PCs exert broad effects on metabolic homeostasis by acting as ligands for nuclear hormone receptors (NRs).[4,10-15] As NR ligands, PCs represent a novel, understudied class of hormone.

Particularly strong evidence supports a role for PCs as ligands of liver receptor homolog-1 (LRH-1). LRH-1 is an orphan NR that regulates cholesterol homeostasis, metabolism, proliferation, and intestinal inflammation and has garnered attention as a novel therapeutic target for diseases such as diabetes, cancer, and inflammatory bowel diseases.[16-22] LRH-1 binds a wide range of PLs *in vitro,* and medium-chained, saturated PCs activate it exogenously.[16,23] Moreover, several models have shown a relationship between endogenous PC levels and LRH-1 activity. Diet-induced depletion of PCs in mice induces an "antagonist" pattern of gene expression in the liver similar to LRH-1 knockout mice.[24] Similarly, diet-induced depletion of PCs in *C. elegans* inhibits the worm LRH-1 ortholog, causing fat accumulation that is rescued by PC agonists.[25] In human hepatocytes, LRH-1 senses PCs generated via methyl metabolism to control beta-oxidation of fatty acids and mitochondrial biogenesis.[26] Finally, oral administration of dilauroylphosphatidylcholine (DLPC, PC 12:0/12:0) induces potent anti-diabetic effects in mouse models of insulin resistance. The anti-diabetic effects are LRH-1-dependent and occur via repression of *de novo* lipogenesis in the liver.[16]

The sensitivity of LRH-1 to PC levels suggests a regulatory circuit connecting PC availability to LRH-1-controlled gene expression. However, this circuit has been difficult to elucidate. Natural PCs are insoluble and rapidly metabolized, and unlikely to be LRH-1-selective, which makes them difficult to work with in the laboratory. These poor pharmacological properties also limit the use of PCs as therapeutics. We therefore designed a set of "PL-mimics" by fusing PL headgroups (or phosphate

bioisosteres) to the synthetic LRH-1 agonist RJW100 (Figure 1a-b).[27] These hybrid molecules contain the hexahydropentalene (6HP) core from RJW100, appended with a polar moiety that mimics a PC headgroup at position R^4 (Figure 1a-b).[27] Based on structural analyses, we hypothesized that the modified R^4 groups would make similar interactions to PCs in the LRH-1 binding pocket and stimulate receptor activity. Indeed, the agonists activate LRH-1 robustly *in vitro* and promote strong patterns of coregulator protein recruitment. We present new crystal structures showing that the agonists are anchored deeply in the pocket via the 6HP core and that the added polar groups make PL-like contacts at the mouth of the pocket as designed. The best of this class is active *in vivo,* suppressing lipogenic genes in the liver and inducing intestinal anti-inflammatory genes in separate mouse studies. Anti-inflammatory effects in the gut profoundly reduce inflammation and weight loss in a murine model of colitis. This work demonstrates that strategic targeting of the PC binding site improves activity, elucidates the mechanism of action of these compounds, and provides the first *in vivo* evidence of efficacy in colitis for a small molecule modulator of LRH-1.

Results

Structure-guided design of PL-mimics.

Crystal structures of LRH-1 bound to PLs depict an unusual ligand binding mode.[12-15,28] Whereas most NR ligands are fully engulfed within the binding pocket, PLs bind LRH-1 with a portion of the headgroup protruding into the solvent (Figure 1a). Lipid phosphates coordinate polar residues near the pocket mouth, while the acyl chains line the pocket interior, making numerous hydrophobic contacts (Figure 1a). We previously focused on strengthening deep pocket interactions made by RJW100, resulting in the discovery of the potent agonists 6N and 6Na (Figure 1c).[29,30] We used an alternative approach to design the PL-mimics, seeking to promote interactions near the mouth of the pocket. Notably, the alkyl "tail" of RJW100 (position R^4) overlaps with the PL fatty acyl chains and follows a

trajectory toward the pocket mouth (Figure 1a).[27] Based on this observation, we synthesized sets of compounds modified at R^4 with alkyl tails of varied lengths at that terminate in polar, PL-mimicking groups (Figure 1b).[27]

Modifications improve binding affinity and activity.

The addition of a phosphorylcholine (PhC) or carboxylic acid (CA) to position R^4 on the RJW100 scaffold dramatically increases LRH-1 transcriptional activity, depending on the length of the alkyl linker connecting the bicyclic core to the modified group.[27] Compounds containing linkers of 9-10 carbons are the strongest activators for both classes, increasing E_{max} nearly two-fold over RJW100 (Figure 1e). The optimal linker is 18-20 Å from the bicyclic core to the terminal polar group for the PhCs and 15-17 Å for the CAs (Figure 1d, Table S1).[27] Compounds with short alkyl linkers (4-5 carbons) do not significantly activate the receptor above baseline at doses up to 30 μM,[27] and diverse modifications elsewhere on the RJW100 scaffold[29] affect potency (EC_{50}) but rarely increase E_{max} (Figure 1e). The PL-mimicking groups also improve binding affinity in a linker length-dependent manner (Figure 1f-g, S1-S3). PhCs and CAs with longer linkers (9-11 carbons) have the highest affinities, with K_i values between 2-11 nM (Figure 1f-g, Table S1). To test whether the improved affinity and activity are caused by the longer alkyl linker or the terminal polar group, we synthesized and tested a set of diols (terminally hydroxy-modified at R^4) with varying linker lengths (Figure 1d). The diols bind and activate LRH-1 similarly to RJW100 regardless of linker length, suggesting that the charged polar group is the driver of the improved properties (Figure 1d, 1h, S3-S4). Together, these data suggest that PL-mimicking groups form productive interactions with LRH-1, greatly increasing transcriptional output.

Structural basis for improved binding and activity.

To understand the mechanism of action of the PL-mimics, we determined X-ray crystal structures of the LRH-1 LBD bound to either 10CA or 9PhC at resolutions of 2.3 and 2.55 Å, respectively

(Figure 2a-b, Table S2). Both structures depict the ligand bound at a single site in the ligand binding pocket (Figure 2a-b). The peptide from the TIF2 coregulator, added to stabilize the complex, is bound at the activation function surface (AFS), comprised of portions of helices 3, 4, and the activation function helix (AF-H, Figure 2a-b).

The electron density surrounding the ligands unambiguously indicates their positions in the ligand binding pocket, including the extended alkyl linkers and terminal polar groups (Figure 2c). The agonists' 6HP cores, styrene substituents and hydroxyl groups adopt nearly identical positions in the deep pocket to RJW100 (Figure S5). Remarkably, the alkyl tails of both 10CA and 9PhC extend toward the mouth of the pocket, with the terminal polar groups close to the DLPC phosphate (seen by superposition with PDB 4DOS,[12] Figure 2d). The CA and PhC groups make very similar contacts near the mouth of the pocket as DLPC, including hydrogen bonds with the sidechains of residues Y516 and K520 and with the α-amino group of G421 (Figure 2e-f). The agonists also make a water-mediated hydrogen bond with the α-amino group of L424 via the CA and phosphate groups (also made by DLPC), strengthening their associations with the pocket mouth. Molecular dynamics simulations (MDS) with the 10CA structure predict that the interactions with Y516 and K520 persist for 50.2% and 37.6% of a 1 µs simulation, respectively. This is similar to DLPC, which interacts for 49.4% of the time with Y516 and 33.2% with K520. The interaction with the backbone amide of G421 is less stable for 10CA than DLPC (27.0% of the simulation *versus* 48.1% for DLPC).

We were particularly interested in how the PL-mimics affect receptor conformation near the mouth of the pocket, since flexibility there is important for allosteric signaling by DLPC.[23] Specifically, the helix 6/ β-sheet region is used to sense ligands and communicate with the coregulator binding surface to recruit appropriate coregulator proteins.[23] PL binding expands the pocket mouth relative to apo LRH-1 via a ~3 Å displacement of helix 6 by the sn1 acyl chain.[31,32] 10CA and 9PhC expand the pocket

mouth through a different mechanism. They do not shift helix 6; instead, they displace the C-terminus of helix 10 by 2.0-2.3 Å relative to apo LRH-1 (from superposition with PDB 4PLD)[23] and 3.5-3.9 Å relative to the LRH-1-DLPC structure, Figure 2g). To form hydrogen bonds with Y516 and K520, the R^4 polar groups of the PL-mimics move toward the C-terminus of helix 10 relative to the DLPC phosphate.

To interrogate the function of the PL-like interactions made in the structures, we mutated key LRH-1 residues and measured the impact on binding affinity and transcriptional activity. Introduction of either a Y516A or K520A mutation decreases DLPC's binding affinity by 40- and 24-fold, respectively, *versus* WT LRH-1 (Figure 2h, S6). We also observe statistically significant reductions in binding affinities for longer-tailed CAs and PhCs for both mutants, with the exception of 9PhC for the K520A mutation (Figure 2h, S6). Compounds with the 6HP scaffold that do not contact these residues (RJW100 and 6N)[32,33] are insensitive or less sensitive to these mutations (Figure 2h, S7). In luciferase reporter assays, mutations to Y516A or K520A do not affect basal activity of LRH-1; however, the Y516A mutation reduces activation by all four agonists by 24-33% relative to WT protein (Figure 2i). Compounds 9CA and 10CA are very poor activators of the K520A mutant, reducing its activation by around 60% *versus* WT LRH-1, while 9PhC and 10PhC activate it equally well as WT protein. Together, these results demonstrate that one or more of the interactions near the mouth of the pocket contribute to the increased affinity and efficacy conferred by the extended polar group at R^4.

Effects on LRH-1 conformation and coregulator recruitment.

To understand how the PL-mimics switch LRH-1 into the active state, we investigated how activating *versus* non-activating CAs affect LRH-1 conformation in solution using hydrogen-deuterium exchange mass spectrometry (HDX-MS). We used four CAs for HDX-MS, two that bind LRH-1 but are inactive (4CA and 5CA) and the two most active agonists in this series (9CA and 10CA). Relative to the inactive compounds, 9CA and 10CA stabilize the LRH-1 activation function surface (AFS), a dynamic

region in the LBD that serves as a binding site for coregulator proteins (Figure 3a, Figure S7). Ligand-induced conformational changes to the AFS tune coregulator associations and modulate transcriptional activity. Compounds 9CA and 10CA stabilize portions of the AFS, including helix 3 and the loop preceding the activation function helix (pre-AF-H loop) relative to the shorter-tailed CAs (Figure 3a-c). 10CA also stabilizes the AF-H and part of helix 4 relative to 4CA (Figure 3a-b).

The stabilization of the AFS observed with HDX-MS suggests that 9CA and 10CA may affect coregulator associations. To test this, we conducted coregulator profiling using the Microarray Assay for Real-time Coregulator-Nuclear Receptor Interactions (MARCoNI), a microarray that quantifies associations of 64 coregulators from a library of 154 peptides containing NR interaction motifs.[34] We first investigated how long- *versus* short-tailed agonists affect coregulator binding to the LRH-1 LBD, using the same CAs as the HDX-MS experiments. Since LRH-1 copurifies with PL from *E. coli*, thought to act as weak agonists,[12-14] we generated apo LRH-1 LBD by stripping the ligands and refolding the receptor[12] (Figure S9). Apo LRH-1 LBD preferentially binds peptides from known LRH-1 corepressors (*i.e.* nuclear receptor corepressor 1 (NCOR1), nuclear receptor subfamily 0 group B member 1 (NR0B1, also called DAX-1), and nuclear receptor subfamily 0 group B member 2 (NR0B2, also called SHP) (Figure S9). The strongest interactor is NFKB inhibitor beta (IκBβ, Figure S9), a direct repressor of the retinoid X receptor[35] that has not been previously reported to bind LRH-1. Both 9CA and 10CA disrupt many of the strongest coregulator interactions with apo-LRH-1 (*i.e.* IκBβ, NCOR1, and transcriptional cofactor of c-*fos* (TREF1)), while strongly recruiting a specific complement of coregulators (*e.g.* ligand dependent nuclear receptor corepressor (LCOR), nuclear receptor coactivator A1 (NCOA1) and nuclear receptor coactivator A3 (NCOA3), Figure 4a). In contrast, 4CA and 5CA have much weaker effects on coregulator associations (Figure 4a). These results suggest that the longer-tailed agonists promote conformational changes to the LBD that affect coregulator recognition of the AFS, consistent with observations from HDX-MS.

In addition to demarking differences between active and inactive compounds, the coregulator recruitment pattern of 9CA and 10CA is also distinct from agonists in different classes. This is seen through comparison to MARCoNI results with 6N and 6N-aniline (6Na), which share the RJW100 core scaffold but are modified elsewhere on the molecule (Figure 1b).[35,36] Unsupervised hierarchical clustering of the data shows a striking separation by ligand class: the most structurally similar ligands cluster together (Figure 4b). The close relationship between 9CA and 10CA in the clustering analysis appears to be due to common effects on coregulator dissociations. This distinguishes them from 4CA, which exhibits an otherwise similar (albeit weaker) pattern of coregulator associations to the longer-tailed compounds (Figure 4b). Coregulator recruitment by 6N and 6Na is weak relative to the longer-tailed CAs, but it also displays a different pattern: for example, 9CA and 10CA promote dissociation of 16 coregulator peptides in common, while 6N and 6Na affect a distinct set of five coregulator peptides (Figure 4c).

Many of the observations from the experiment with isolated LBD are recapitulated in a MARCoNI study using FL-LRH-1. This is not a direct correlate to the LBD experiment, since apo-FL protein was unstable, and FL-LRH-1 in this experiment was bound to copurifying *E. coli* PL. Interestingly, the recombinant FL-LRH-1 exhibits a nearly identical coregulator binding pattern to untreated apo-LBD (Figure S9). The FL protein also responds very similarly to 10CA, strongly recruiting peptides from LCOR, NCOA1, and SHP and strongly dissociating IκBβ, NCoR1, and TREF (Figure S9). A total of 85% of the peptides affected by at least 1.5-fold over baseline by 10CA in the LBD experiment are also altered by more than 1.5-fold with FL-LRH-1 (Figure 4d). As in the LBD experiment, the effects of 6N are relatively weak and mainly involve coregulator dissociation, including IκBβ and several canonical LRH-1 corepressors (*e.g.* NCOR1, PROX1, SHP, and DAX-1, Figure S9). Differences between 10CA and 6N are more apparent with FL-LRH-1 than LBD: 22 peptides are recruited by one compound and displaced by the other (Figure 4e). These striking differences in patterns of coregulator recruitment by 10CA *versus*

6N are indicative of distinct ligand-induced conformational changes at the LRH-1 AFS, demonstrating that receptor allostery is tunable through ligand modifications. These studies also reveal the strong effects on coregulator recruitment driven by the strategic addition of a PL-mimicking group.

10CA reduces expression of lipogenic genes in the liver.

LRH-1 is highly expressed in the liver, where it regulates bile acid biosynthesis, ER-stress resolution, and *de novo* lipogenesis.[16,17,37] We tested whether 10CA, one of the most active of the new compounds in luciferase assays, could activate endogenous LRH-1 in Huh7 hepatocytes. A 24-hour treatment of 10CA dose-dependently upregulates known LRH-1 transcriptional targets SHP (*NR0B2*) and polo-like kinase 3 (*PLK3*). 10CA also downregulates targets involved in *de novo* lipogenesis, including sterol regulatory element-binding protein 1 (*SREBPF1,* also called SREBP1-c), acetyl-CoA carboxylase 2 (*ACACB*), fatty acid synthase (*FASN*), and stearoyl-CoA desaturase-1 (*SCD1*) (Figure 5a). Interestingly, downregulation of these lipogenic genes in the liver is associated with LRH-1-dependent antidiabetic effects by DLPC.[16]

To determine whether 10CA can activate LRH-1 in the liver *in vivo*, we overexpressed human LRH-1 (hLRH-1) in C57BL/6J mice using AAV8 adenovirus. The overexpression strategy was chosen because 10CA and analogs are poor activators of mouse LRH-1 in luciferase reporter assays (data not shown). Two weeks after viral infection, mice were treated with 10CA at 0.1, 1, or 10 mg/kg in a series of five intraperitoneal injections spanning three days (Figure 5b). Overexpression of hLRH-1 was verified by qRT-PCR (Figure 5c), and agonist-induced gene expression changes in the liver were assessed by Nanostring.[38] The most prominent effect of 10CA treatment is the downregulation of lipogenic genes (Figure 5d-e). The affected genes were the same as those downregulated in Huh7 cells (*FASN, SREBPF1, ACACB,* and *SCD1*). The downregulation was dependent on hLRH-1 expression, since they were unchanged in mice not expressing hLRH-1 (Figure S10).

Efficacy of 10CA in organoid and murine models of colitis

LRH-1 is a novel therapeutic target for inflammatory bowel diseases such as ulcerative colitis (UC), a chronic disease characterized by inflammation of the colon and decreased integrity of the intestinal epithelium.[39] LRH-1 regulates local glucocorticoid production in the intestine that promotes cell survival, which is important for maintenance of the intestinal epithelial barrier.[40-43] Loss of LRH-1 function in mice decreases glucocorticoid production in the intestinal epithelium and decreases expression of *Cyp11a1* and *Cyp11b1*, genes that regulate corticosterone production.[40] These defects are rescued by overexpression of hLRH-1.[43] We therefore investigated efficacy of 10CA in UC. We began with an *in vitro* model, using organoids derived from intestinal crypts of humanized LRH-1 mice (enteroids). In these enteroids, hLRH-1 is expressed in the context of conditional deletion of endogenous LRH-1 in the intestinal epithelium,[43] and they mimic UC when stimulated with tumor necrosis factor alpha (TNF-α) to induce inflammation.[29,43,44] Overnight treatment with 10CA induces expression of *Cyp11a1* and *Cyp11b1*, increases expression of the anti-inflammatory cytokine *Il-10*, and decreases expression of pro-inflammatory cytokines *Il-1B* and *TNFa* (Figure 6a-c). These changes in gene expression require the expression of hLRH-1, since they are not observed in epithilium-specific LRH-1-deficient enteroids (Figure S11). Therefore, 10CA strongly upregulates LRH-1-controlled steroidogenesis in enteroids with concomitant anti-inflammatory gene expression changes.

To test efficacy of 10CA *in vivo,* we utilized a dextran sulfate sodium (DSS)-induced murine model of UC, using epithelium-specific humanized LRH-1 mice. Administration of DSS rapidly damages the intestinal epithelium, resulting in intestinal inflammation and compromised barrier function.[45] Mice received seven days of DSS treatment, followed by five days of daily intraperitoneal injections of 10CA or vehicle. DSS administration caused rapid weight loss in both groups beginning around day 5, typical for this disease model.[46] Vehicle-treated animals lost an average of 8.6% initial body weight by the end of the study (Figure 6d). In contrast, mice treated with 10CA began re-gaining weight on day 9 and were

within 1% of baseline at the end of the study (Figure 6d). 10CA-treated mice had markedly improved scores for disease activity, which quantify severity of symptoms such as diarrhea and blood in the stool (Figure 6e), and scores for histology and gross morphology, which quantify inflammation, tissue damage, and crypt loss in the colon (Figure 6e). Representative colonic tissue sections illustrate the striking differences between 10CA-treated and control mice, with examples of crypt loss highlighted in yellow (Fig. 6f-g). This is the first LRH-1 small molecule agonist to show *in vivo* efficacy in a model of colitis, demonstrating the potential of targeting LRH-1 for treatment of this chronic disease.

Discussion

The discovery that PCs act as nuclear receptor ligands has illuminated the potential for novel signaling axes connecting PC metabolism with gene expression. Compelling evidence from gain and loss of function studies connects PC availability to LRH-1-controlled transcriptional programs involving lipid and methyl metabolism. A close relationship between PC generation via the one-carbon pathway and the response of LRH-1 to dietary PCs has led to the intriguing hypothesis that LRH-1 senses PCs as a proxy for nutrient availability. Likewise, PCs have anti-inflammatory effects in the intestinal mucosa that are not fully explained by their physical role in this tissue.[47-50] The agonists described herein provide tools to probe a potential LRH-1-PC regulatory circuit, which is challenging to elucidate with natural PCs due to their lability and promiscuity.[51]

Crystallographic data reveals very different binding modes of natural PL and the synthetic LRH-1 modulator RJW100, with the former making polar interactions near the mouth of the pocket and the latter being anchored in the deep pocket.[31,32] The hybrid PL-mimics were designed with the rationale that appending a polar moiety to an extended R^4 alkyl tail would allow the agonists to interact with both regions of the pocket. With two new crystal structures, we demonstrate that this strategy was successful: the 6HP cores nearly perfectly superpose with RJW100, while the polar groups in the

extended tails form hydrogen bonds with several residues engaged by the DLPC phosphate group (Figure 2). Disrupting these hydrogen bonds via mutagenesis reduces binding affinity and decreases activity of the longer-tailed agonists (Figure 2). Compounds with shorter tails or lacking a charged group at the R^4 terminus are not more active than RJW100, further demonstrating that the PL-mimicking interactions are responsible for the improved binding and activity profiles (Figure 1). HDX-MS experiments show that the longer-tailed CAs stabilize the LRH-1 AFS relative to shorter-tailed CAs (Figure 3). The AFS stabilization is associated with much stronger effects on coregulator recruitment than seen with shorter-tailed CAs, including dissociation of many factors bound by apo-LRH-1 (Figure 4). Together, these data suggest a model in which specific interactions made by the PL-mimicking group promote conformational changes at the AFS that activate the receptor by modulating coregulator associations. Notably, the allostery observed for the PL-mimics is different from that of DLPC, which relies upon flexibility and motion of the region near helix 6.[23] The PL-mimics do not displace helix 6 in the crystal structures (Figure 2), and the flexibility of helix 6 is unchanged in HDX-MS experiments with 9CA and 10CA *versus* shorter-tailed CAs (Figure 3). The agonists therefore mimic PC interactions but act more as hybrids between PCs and synthetic agonists with respect to effects on receptor conformation and allostery. Nevertheless, the PL-mimics recapitulate many gene expression changes made by exogenous DLPC, including downregulation of lipogenic genes in hepatocytes and mouse liver (Figure 5). Downregulation of the same set of lipogenic genes and consequent suppression of *de novo* lipogenesis is thought to be the main mechanism through which DLPC exerts anti-diabetic effects, including reducing liver fat accumulation and improving insulin resistance.[16] This suggests a potential for the new agonists in diabetes and metabolic disorders associated with obesity, which is an ongoing area of research in our laboratories.

LRH-1 is as an important regulator of intestinal cell renewal and local inflammation in the gut.[41,43] One of the most exciting findings in these studies is the strong efficacy in UC *in vivo.* While gain

and loss of function studies have demonstrated the potential of targeting LRH-1 in colitis,[43] and the agonist 6N activates steroidogenic genes in enteroids,[33] this is the first demonstration of a synthetic molecule to exhibit *in vivo* efficacy. In DSS-induced UC, LRH-1 activation by 10CA markedly decreases disease markers, inhibits colonic crypt loss, and ameliorates disease-associated weight loss (Figure 6). Studies in enteroids link this efficacy to anti-inflammatory gene expression patterns (Figure 6). Targeting LRH-1 in UC is a particularly intriguing strategy, as its activation suppresses inflammation locally in the gut.[41,52] UC is commonly treated with corticosteroids, anti-TNFα therapies, or other systemic immunosuppressants that often cause adverse effects associated with immunosuppression in tissues other than the colon[53]. Thus, LRH-1 agonists may offer a more precise approach to UC treatment, reducing the potential for on-target, adverse effects in other tissues.

Together, this work has demonstrated an exciting potential for incorporating PL-mimicking interactions into LRH-1 agonists. The PL-mimics are valuable tools to study LRH-1 activation by ligands and to broaden our understanding of PL-regulated transcriptional programs. They also have potential as therapeutics for diseases associated with aberrant LRH-1 activity, such as diabetes and UC.

Methods

Chemical synthesis. We have previously described the synthesis of the phosphorylcholine derivatives (4PhC-11PhC, also called 12a-12h) and carboxylic acid derivatives (4CA-11CA, also called 13a-13h) modified at the R^4 position of the RJW100 scaffold.[27] Methods for synthesis of diols (4OH-11OH) are described in detail in the supplemental materials. Synthetic methods for RJW100 and RJW100 analogs modified at positions R^1, R^2, or R^3 (compounds 1N-8N; 1X-8X; 9-23, used to generate Figure 2B) have also been published previously.[29]

Cell Culture. Hela and Huh7 cells were purchased from Atlantic Type Culture Collection. Hela cells were cultured in MEMα medium supplemented with 10% charcoal-stripped fetal bovine serum. Huh7 cells

were cultured in DMEM/F12 medium (Gibco) supplemented with 10% fetal bovine serum. Cells were maintained under standard culture conditions.

Reporter gene assays. Hela cells were seeded into 96-well culture plates at 7500 cells/ well and transfected with reporter plasmids and either pCI empty vector or full-length LRH-1-pCI. Reporter plasmids consisted of (1) the pGL3 basic vector containing a portion of the SHP promoter containing the LRH-1 response element cloned upstream of firefly luciferase and (2) a constitutively active vector encoding *Renilla* luciferase used for normalization. Transfections utilized the FugeneHD transfection reagent at a ratio of 5 μl Fugene: 2 μg DNA. Cells were treated with agonists 24 hours after transfection at concentrations indicated in the figure legends. 24 hours after treatment, luminescence was quantified using the DualGlo kit from Promega on a BioTek Neo plate reader. Values for EC_{50} and E_{max} were calculated by fitting data to a three-parameter dose-response curve in GraphPad Prism, v7.

Calculation of Relative Efficacy (RE). This value was used to compare data from luciferase reporter assays that were conducted on different dates by normalizing values to data from the compound RJW100 assessed in parallel experiments. RE was calculated from curve-fitting to data from luciferase reporter assays. To compare the maximum activities of the new compounds to RJW100, we used the formula $(Max_{cpd} – Min_{cpd}) / (Max_{RJW100} – Min_{RJW100})$, where "Max" and "Min" denote the dose response curve maximum and minimum, respectively. A RE of 0 indicates a completely inactive compound, a value of 1 indicates equal activity to RJW100, and values above 1 indicate greater activity.

Protein purification

LRH-1 LBD. LRH-1 LBD (residues 299-541) in the pMSC7 vector was transformed in *E. coli* strain BL21(pLysS) for expression. Cultures were grown at 37 °C in liquid broth to an OD_{600} of 0.6 prior to induction of protein expression with 1 mM isopropyl-1-thio-D-galactopyranoside (IPTG). Cultures were grown for 4 hours at 30 °C following induction. Protein was purified by nickel affinity chromatography

with Buffer A of 20 mM Tris HCl (pH 7.4), 150 mM NaCl, 5% glycerol, and 25 mM imidazole and Buffer B of 150 mM Tris HCl (pH 7.4), 150 mM NaCl, 5% glycerol, and 500 mM imidazole (HisTrap FF; GE Healthcare, Little Chalfront, UK). Protein was incubated with DLPC (4-fold molar excess) overnight at 4 °C, repurified by size exclusion into assay buffer (150 mM NaCl, 20 mM Tris-HCl (pH 7.4), and 5% glycerol, concentrated to approximately 3 mg/mL, and stored at -80 °C until use. The same purification strategy was utilized for protein containing the point mutations described in the text.

Full-length LRH-1 purification. The gene encompassing the full-length LRH-1 (FL-LRH-1; residues 1-495, isoform 1) was codon-optimized for *E. coli,* sub-cloned into a modified PET28b vector with a His-SUMO tag and transformed into *E. coli* strain BL21 (DE3) cells. Cells were grown in LB media at 37 °C to an OD_{600} of 0.5. Protein expression was induced with 0.2 mM IPTG and grown overnight at 16 °C. Cells were harvested by centrifugation and resuspended into lysis buffer containing 20 mM Tris (pH 7.5), 500 mM NaCl, 5% glycerol, 25 mM imidazole, 0.5 mM *tris*(2-carboxyethyl) phosphine (TCEP), and 0.1 mM phenylmethylsulphoyl fluoride (PMSF). Cells were lysed by sonication for 8 minutes and clarified by centrifugation. Protein was purified by nickel affinity chromatography with elution buffer of 20 mM Tris HCl (pH 7.5), 500 mM NaCl, 5% glycerol, 0.5 mM TCEP and 125 mM imidazole (HisTrap FF; GE Healthcare, Little Chalfront, UK). The His-Sumo tag was removed using tobacco etch virus (TEV) protease at 4 °C with dialysis against buffer containing 20 mM Tris (pH 7.5), 500 mM NaCl, 5% glycerol and 0.5 mM TCEP. Ion-exchange chromatography was used to isolate cleaved protein and remove DNA with tandem Hitrap Q-SP columns (GE Healthcare). Protein was flowed through the Q column onto the SP column, from which it was eluted as a single peak using a linear gradient of NaCl from 0.35 M to 1 M. Finally, the protein was further purified to homogeneity by size exclusion chromatography. Functionality of the purified protein was determined by testing its ability to bind DNA containing an LRH-1 response element, and its ability to bind ligand (see "*Ligand binding assay*" for details). DNA binding was measured using fluorescence polarization with a 6-carboxyfluorescein (cFAM)-labeled double-

stranded DNA probe containing the LRH-1 binding element from the CYP7A1 promoter. FL-LRH-1 was titrated against 10 nM FAM-CYP7A1 in buffer containing 20 mM Tris (pH 7.5), 150 mM NaCl, 5% glycerol and 0.5 mM TCEP, with a final volume of 50 µL, and incubated at room temperature for 30 min. Polarization was monitored on a Synergy 4 microplate reader (Biotek, Winooski, VT) at an excitation/emission wavelength of 485/528 nm. Curves were fit using a one-site specific binding equation with baseline-subtraction of protein alone in GraphPad Prism, v7. One biological replicate was conducted with two technical replicates.

Generation of apo LRH-1. To extract lipids from the LRH-1 LBD, 1 mL of purified protein (3 mg) was treated with 3.75 mL of chloroform-methanol solution (1:2 v/v) and vortexed briefly. An additional 2.5 mL chloroform:water solution (1:1 v/v) was added and the mixture was vortexed again. The stripped and unfolded protein was pelleted by centrifugation at 1000 rpm for 10 minutes. The resulting protein pellet was dissolved into 0.5 mL of buffer containing 50 mM Tris (pH 8.0), 6 M guanidine hydrochloride and 2 mM DTT. Protein was refolded by fast dilution at 4 °C into 25 mL of buffer containing 20 mM Tris (pH 8.5), 1.7 M urea, 4% glycerol and 2 mM DTT. The final urea concentration was adjusted to 2 M, and the protein was concentrated to ~ 1.5 mL, followed by overnight dialysis against PBS containing 2 mM DTT at 4 °C. Refolded protein was purified by size exclusion chromatography to remove aggregates and remaining unfolded protein, and ligand binding ability was verified by fluorescence polarization as described below.

Mutagenesis. Mutations were introduced to LRH-1 in the pMSC7 and pCI vectors using the Quikchange Lightning Site-Directed Mutagenesis Kit as directed by the manufacturer (Agilent). Constructs were sequenced prior to use in binding or activity assays.

Ligand binding assay. All assays were conducted in black, polystyrene, non-binding surface 384-well plates (Corning Inc., Corning, NY) with 30 µL volumes in assay buffer (150 mM NaCl, 20 mM Tris-HCl pH

7.4, 5% glycerol). Binding affinity of the fluorescein amidite (FAM)-labeled probe (6N-FAM) for WT and mutant LRH-1 was determined by titrating purified protein in the presence of 10 nM 6N-FAM, as previously described.[54] The affinity of the probe for WT and mutant LRH-1 LBD from these initial experiments was used to determine probe and protein concentrations for competition experiments with unlabeled agonists. Competition assays were conducted with 10 nM 6N-FAM (10, 0.6, and 1.1 times the K_d of wildtype, K520A, and Y516A LRH-1, respectively, for 6N-FAM). For protein concentration, 5, 10, and 15 nM wildtype, K520A, or Y516A LRH-1 were used, representing 50-80% of the B_{max} from the 6N-FAM binding curves for each protein variant. Assay conditions were validated using unlabeled compound 6N. Competition experiments used unlabeled agonists at a concentration range of 200 pM-200 μM. Plates were incubated overnight at 4 °C and centrifuged at 2,000 x g for 2 minutes before polarization measurement. Polarization was monitored on a Neo plate reader (Biotek, Winooski, VT) at an excitation/emission wavelength of 485/528 nm. The experiment was conducted twice in quadruplicate, and GraphPad Prism version 7 was used to analyze compiled data. Data were first baseline subtracted with the lowest concentration of competitor as the baseline. To compare the ability of each competitor to displace the 6N-FAM probe from LRH-1, data were then normalized to the unlabeled 6N competition curve, as 6N completely competes the 6N-FAM probe, such that a baseline of 0 represents complete competition of the 6N-FAM probe for a given agonist. Finally, data were fit using a one-site, fit K_i curve in GraphPad Prism. This equation fits the K_i of the unlabelled competing ligand using the EC_{50} of the competition curve, the concentration of the fluorescent probe, and the K_d of the probe for each receptor, as follows:

Equation 1: Calculating the EC_{50} of the competing ligand.

Y=Bottom + (Top-Bottom)/(1+10^(X-LogEC_{50}))

Equation 2: Calculating K_i from EC_{50}, probe concentration, and probe K_d.

$\log EC_{50}=\log(10^{\log K_i}*(1+[\text{Probe, nM}]/\text{Probe Kd, nM}))$

Mutants were normalized to their respective unlabeled 6N competition curves, which had different shifts in polarization than wildtype. To compare K_i values for wildtype versus K520A and Y516A mutants, two-way ANOVA was conducted followed by Dunnett's test for multiple comparisons (GraphPad Prism v7).

Hydrogen-deuterium exchange mass spectrometry (HDX-MS). Following affinity purification and removal of the His-tag as described above, LRH-1 LBD protein was repurified by size exclusion chromatography into an assay buffer of phosphate-buffered saline, pH 7.5, plus 5% glycerol. Protein aliquots (2 mg/ml) were incubated with carboxylic acid derivatives 4CA, 5CA, 9CA, or 10CA at 5-fold molar excess, overnight at 4 °C. Samples were diluted 1:7 (v/v) in labeling buffer to initialize exchange reactions (same as the protein buffer but containing 99.9 % D_2O instead of H_2O). The reactions were quenched after 0, 10, 100, 1000 and 10000 seconds by adding equal volume of precooled quenching buffer (100 mM phosphate, 0.5 M tris(2-carboxyethyl) phosphine, 0.8% formic acid, and 2% acetonitrile, pH 2.5). Reactions for each sample at each time point were performed in triplicate. Quenched samples were passed through an Enzymate BEH pepsin column (Waters Corp, Milford, MA). Fragmented peptides were separated by an C18 UPLC column and analyzed by a Q-Tof Premier mass spectrometer. ProteinLynx Global SERVER™ (PLGS) was used to identify peptides by database searching of LRH-1 LBD sequence. The HDX-MS data were further processed using DynamX (v3.0) and the differential HDX between ligand-bound states was calculated by comparing the relative fractional uptake for each residue at given time.

In vitro NR-coregulator recruitment by MARCoNI

Experiment with LRH-1 LBD: Assay mixes consisted of 50 nM purified His-LRH-1 LBD (either in the apo state or pre-loaded with compounds), 25 nM ALEXA488-conjugated penta-His antibody (Qiagen # 35310), 50 µM DTT, 20mM Tris (pH 7.4), 250mM NaCl and 0.5 mM TCEP.

Experiment with FL-LRH-1: Assay mixes of 50 nM His-SUMO-hLRH-1-FL (bound to copurifying PL from *E. coli* or preloaded with compound during purification), 25 nM ALEXA488-conjugated penta-His antibody (Qiagen # 35310), 50 µM DTT, and 10 µM freshly added compound (or 2% DMSO) were made in 20mM Tris(pH 7.4), 250mM NaCl and 0.5 mM TCEP and stored on ice.

LRH-1 in the assay mixes was analyzed by applying Microarray Assay for Real-time Coregulator Nuclear Receptor Interaction (MARCoNI), using PamChip #88101 with 154 unique coregulator sequences, as described previously.[54] In short, each condition was tested using three technical replicates (arrays), and LRH-1 binding to each coregulator motif was quantified using BioNavigator software (PamGene). The compound-induced log-fold change (LFC) of LRH-1 binding to each coregulator peptide and statistical significance (Student's t-test) were calculated and visualized using R software (R Core Team, 2017). Compound and interaction (dis)similarity were calculated by Hierarchical Clustering on Euclidean Distance and Ward's agglomeration. Upset plots were generated using the R package UpSetR v1.4.0.[56]

Crystallography. 6X-His-LRH-1 LBD was expressed and purified by nickel affinity chromatography as described above. The His tag was cleaved overnight at 4 °C using TEV protease with dialysis against buffer containing 150 mM NaCl, 5% glycerol, and 20 mM Tris HCl (pH 7.4). Cleaved protein was isolated using nickel affinity chromatography. To generate protein-ligand complexes, purified protein was incubated overnight at 4 °C with 4-5-fold molar excess of ligand. Complexes were purified by size exclusion chromatography into crystallization buffer consisting of 150 mM NaCl, 100 mM ammonium acetate (pH 7.4), 1 mM DTT, and 1 mM EDTA, 2 mM 3-[(3-cholamidopropyl)dimethylammonio]-1propanesulfonic acid (CHAPS) and then incubated with 4-fold molar excess of Tif2 peptide for two

hours at room temperature (Tif2 peptide sequence was H_3N-KENALLRYLLDK-CO_2^-). Crystallization conditions for each complex were as follows:

LRH-1-10CA-Tif2: The LRH-1-10CA-TIF2 complex was concentrated to 5 mg/mL and screened using the Classics screen (Qiagen) and a Phoenix Liquid Handler (Art Robbins Instruments) in 96-well sitting drop plates. Crystals were generated at room temperature in 0.4 M N/K tartrate.

LRH-1-9PhC-Tif2: Crystals were generated by soaking into LRH-1-10CA-Tif2 crystals. First, we generated LRH-1-10CA-Tif2 crystals in larger drops by microseeding, using the LRH-1-10CA-Tif2 crystals described above as seed stocks. Fresh LRH-1-10CA-Tif2 complex was concentrated to 5.2 mg/mL, and the seed stock was added to the protein at a dilution of 1:100. The complex was then crystallized by sitting drop vapor diffusion at 4 °C, in drops containing 1 μl protein/seed stock plus 2 μl crystallant. The crystallant was 9-19% tert-butanol, 0-6 % glycerol, 0.1 M tri-sodium citrate pH 4.6. The 9PhC ligand was soaked into the crystal drops at 1 μM (~1% DMSO) for two days, and 1 μM 9PhC was also added to the cryoprotectant.

Structure Determination. Crystals were flash-frozen in liquid nitrogen using a cryoprotectant of 30% glycerol in crystallant. Data were collected remotely from Argonne National Laboratory (South East Regional Collaborative Access Team, Lemont, IL) using the 22ID beamline. Data were processed and scaled using HKL2000[57] and phased by molecular replacement using Phaser-MR in Phenix[57] with PDB 5L11 as the search model. For the 9PhC structure, the 10CA structure was used as the search model. Coot[59] and Phenix.refine[57] were used for model building and refinement, respectively. Figures were constructed using Pymol.[60] Ligplot+[61] was used to identify residues interacting with the ligands. Measurements to determine displacement of helix 10 were between C-alphas of residue N523 for each protein.

Molecular dynamics simulations.

Model construction:

For model construction, two crystal structures of LRH-1 LBD in complex with Tif2 were used. These were (1) PDB 7JYD (10CA ligand) and (2) PDB 4DOS (DLPC). The structures were modified at the N and C termini so that they included residues 300-540 of LRH-1 and residues 742-751 of the Tif2 peptide. Missing residues within this protein sequence were added, as well as missing protein side chains.

Simulations:

All complexes were solvated in an octahedral box of TIP3P water with a 10 Å buffer around the complex. Na^+ and Cl^- ions were added to neutralize the complex and achieve physiological conditions (150 mM sodium chloride). All systems were generated with the Xleap module of AmberTools,[62] using the ff14SB force field.[63] Parameters for all ligands were obtained using the Antechamber module[64] of AmberTools. All minimizations and simulations were performed with Amber16.[62] Using a minimization protocol of 5000 steps of steepest descent followed by 5000 steps of conjugate gradient, systems were minimized in an iterative manner: i) with 500 kcal/mol.$Å^2$restraints on all atoms; ii) with 500 kcal/ mol.$Å^2$ restraints on restraints retained on ligand and peptide atoms; iii) with restraints removed from all atoms. Following minimization, systems were heated from 0 to 300 K using a 100-ps run with constant volume periodic boundaries and 5 kcal/mol.$Å^2$ restraints on all protein and ligand atoms. Equilibration was performed using a 12-ns MD run with 10 kcal/mol.$Å^2$ restraints on protein and ligand atoms using the NPT ensemble. Restraints were reduced to 1 kcal/mol.$Å^2$ for an additional 10 ns of equilibration. All restraints were removed, and production runs were performed for 1 µs in the NPT ensemble. A 2-fs time step was used for all simulations. All bonds between heavy atoms and hydrogens were fixed with the SHAKE algorithm.[65] A 10-Å cutoff was used for nonbonded interactions. Long range electrostatics were evaluated using Particle Mesh Ewald (PME). For analysis, frames were obtained at 20 ps intervals from each simulation. The CPPTRAJ module[66] of AmberTools was used for structural averaging of MD trajectories and distance calculations.

Agonist treatment and RNA extraction in Huh7 cells. Huh7 cells were plated in 6-well plates at $5x10^5$ cells/well. After 24 hours, cells were treated with vehicle (0.1% DMSO in media) or indicated concentrations of 10CA. Cells were collected for RNA after 24 hours of treatment. RNA extraction was performed using the RNAeasy Mini RNA extraction kit (Qiagen).

Animals. Experimental protocols for the AAV8 overexpression study were approved by the Institute for Animal Care and Use Committee at T3 Laboratories and Emory University and conformed to the Guide for the Care and Use of Laboratory Animals, published by the National Institutes of Health (NIH Publication No. 86-23, revised 1996), and with federal and state regulations. C57BL/6J mice (male; 10-12 weeks of age) were purchased from Jackson Labs (Bar Harbor, ME, USA). Mice were housed at room temperature in a 12-hr light/12-hr dark vivarium, with *ad libitum* access to food and water.

For the experiments involving enteroids and DSS, the study protocol was approved by the Animal Care and Use Committee of the Baylor College of Medicine and was in accordance with the Guide for the Care and Use of Laboratory Animals [DHHS publication no. (NIH) 85-23, revised 1985, Office of Science and Health Reports, DRR/NIH, Bethesda, MD 20205]. Animals were housed and bred in a specific pathogen free (SPF) facility. An inducible intestinal epithelia cell (IEC) knockout line was created by crossing animals harboring CreERT2 under control of the villin promoter with LRH-1 floxed (LRH-$1^{f/f}$)animals and bred to homozygosity (LRH-1 KO, LRH-$1^{f/f}$;Villin-Cre+). The humanized LRH-1 line (LRH-$1^{f/f}$;hLRH-$1^{\Delta\Delta}$;Villin-Cre+) was generated with Rosa26-LoxP-STOP-LoxP-hLRH-1 animals, crossed into our LRH-1 KO line, which conditionally overexpresses hLRH-1 in the intestinal epithelium with the knockout of endogenous mLRH-1.

Viral overexpression and drug treatment. Adeno-associated virus serotype 8 (AAV8) expressing N-terminal Avi-tagged, human LRH-1 was obtained from Vector Biolabs (Malvern, PA, USA). C57BL/6J mice were administered $1x10^{12}$ genome copies (GC)/mL via femoral vein injection. All experiments were conducted two weeks after virus treatment. Mice were administered 0.1, 1.0, or 10 mg/ kg of 10CA or vehicle (5% ethanol in sunflower oil) via intraperitoneal injection five times over a 3-day period. Mice

were treated each morning and evening for two days and on the morning of day 3. Mice were euthanized on day 3, approximately four hours after the final drug treatment. Mouse liver tissue was collected and flash-frozen in liquid nitrogen at the time of euthanasia. Tissue samples were subsequently stored at -80 °C. To extract RNA, liver samples were cryo-pulverized in liquid nitrogen, then homogenized in TRI® Reagent (Invitrogen) and RNA was extracted using the TRI® Reagent protocol followed by miRNAeasy Mini RNA extraction kit (Qiagen). A portion of the RNA was retained for NanoString analysis, and a portion was subjected to qRT-PCR to verify overexpression of hLRH-1. Reverse transcription was performed using the High Capacity cDNA Reverse Transcription Kit (Applied Biosystems). qPCR was performed using the *Power* SYBR™ Green PCR Master Mix (Applied Biosystems) and run on a StepOnePlus™ Real-Time PCR instrument (Applied Biosystems). Data were analyzed via the $\Delta\Delta C_t$ method, with *Tata binding protein* (*Tbp*) serving as the reference gene. Primers for hLRH-1 detection by qPCR were CTTTGTCCCGTGTGTGGAGAT (forward) and GTCGGCCCTTACAGCTTCTA (reverse) and for Tbp were TGCACAGGAGCCAAGAGTGAA (forward) and CACATCACAGCTCCCCACCA (reverse).

NanoString Gene Expression Analysis. RNA was extracted from liver tissue as detailed above. RNA concentration was determined from OD values on a Nanodrop 1000. Sample profiles were assessed on a 2100 Bioanalyzer Instrument (Agilent) using the RNA 6000 Nano (25ng/ul – 1,000ng/ul) or Pico assay (0.5ng/ul – 20ng/ul). All RNA Integrity (RIN) scores were >9.0. 25ng of total RNA was hybridized with biotin labeled capture probes and fluorescently labeled reporter probes from NanoString Technologies, Inc. for 18 hours at 65 °C. Following hybridization, samples were injected into a NanoString SPRINT cartridge and loaded onto the nCounter SPRINT Profiler instrument where excess capture probe and reporter probe were removed, and hybridized mRNAs were immobilized for imaging. Following image acquisition, mRNA counts were extracted from raw RCC files using nSolver™ data analysis software (ver.4.0, NanoString Technologies, Inc.) and exported as .csv files for further analysis. One-way ANOVA followed by pairwise t-tests were used to determine statistical significance.

Humanized LRH-1 Mouse Intestinal Enteroid Culture. Intestinal crypt culture (enteroids) were derived from LRH-1 KO (LRH-1$^{f/f}$;Villin-Cre+), and hLRH-1 (LRH-1$^{f/f}$;hLRH-1$^{\Delta\Delta}$;Villin-Cre+) male mice (6−8 weeks old). Briefly, the small intestine was isolated and flushed with ice-cold PBS, opened longitudinally, then cut into 1−2 mm pieces. Intestinal fragments were incubated in an EDTA-containing solution (4 mM) at 4 °C for 60 min on a tube rocker. The intestinal fragment suspension was fractionated by vertical shaking manually and crypt-containing fractions passed through a 70 µm cell strainer for plating in Matrigel. The crypt-Matrigel suspension was allowed to polymerize at 37 °C for 15 min. Intestinal organoids were grown in base culture media (Advanced DMEM/F12 media, HEPES, GlutaMax, penicillin, and streptomycin) supplemented with growth factors (EGF, Noggin, R-spondin, R&D Systems), B27 (Life Technologies), N2 (Life Technologies), and N-acetyl cysteine (NAC, Sigma). Intestinal enteroids were passaged every 3 days. Established LRH-1h enteroids were treated with mouse TNF-α overnight to provoke inflammatory changes, then treated with vehicle (DMSO) or compound 10CA (1 µM) overnight. Following the treatment, enteroid tissues were harvested for real-time PCR.

RNA Isolation and RT-qPCR. Intestinal enteroids were washed in ice cold PBS and suspended in Trizol solution (Sigma). RNA was isolated with RNeasy spin columns (Qiagen). DNAse-treated total RNA was used to generate cDNA using Superscript II (Quanta). Sybr green-based qPCR (Kapa Biosystems) was performed on a Roche LightCycler 480 II with primers as shown below. The $\Delta\Delta C_t$ method was used for calculating gene expression fold changes using Rplp0 (ribosomal protein, large, P0, known as 36B4) as the reference. Primer sequences are shown in Table 1 below.

Table 1. List of primers for qRT-PCR with enteroids.

Gene	Forward Primer (5’ → 3’)	Reverse Primer (5’ → 3’)
m/hLRH-1	GTGTCTCAAT TTAAAATGGT GAATTACTCC TATGATGAAG	AAT AAGTTTGGGC CAATGTACAA GAGAGACAGG

Cyp11a1	GCTGGAAGGTGTAGCTCAGG	CACTGGTGTGGAACATCTGG
Cyp11b1	primers purchased from QuantiTect, Qiagen (NM_001033229, catalog # QT01198575)	
IL-10	GCCTTATCGGAAATGATCCAGT	GCTCCACTGCCTTGCTCTTATT
IL-1β	primers purchased from QuantiTect, Qiagen (NM_008361, catalog # QT01048355)	
TNFα	CCAGAAAAGACACCATGAGCAC	GGGCCATAGAACTGATGAGAGG
Rplp0(36B4)	GAAACTGCTGCCTCACATCCG	GCTGGCACAGTGACCTCACAC

Dextran sulfate sodium (DSS) induced colitis model: hLRH-1 mice (8 weeks old) were administered 2.5% DSS w/v in drinking water for 5 days, followed by regular water for 7 days. The 10CA (1mg/kg) or vehicle (0.9% normal saline) were administered by daily intraperitoneal injection beginning on D6 for seven days, during which body weights were monitored daily. At the end of treatment, disease activity scores were assessed according to Table S3. For colon histological analysis, the colon was divided into three segments (proximal third, middle third, and distal third). Each segment was embedded in paraffin, sectioned at 5 µm, and stained with hematoxylin and eosin. Histological analysis was performed in the Cellular and Molecular Morphology Core of the Digestive Disease Center at Baylor College of Medicine. The sections were blindly scored using a standard histologic colitis score. Three independent parameters were measured: severity of inflammation (0–3: none, slight, moderate, severe), depth of injury (0–3: none, mucosal, mucosal and submucosal, transmural), and crypt damage (0–4: none, basal one-third damaged, basal two-thirds damaged, only surface epithelium intact, entire crypt and epithelium lost). The score of each parameter was multiplied by a factor reflecting the percentage of tissue involvement (×1, 0–25%; ×2, 26–50%; ×3, 51–75%; ×4, 76–100%) averaged per colon.

Acknowledgements

The authors thank the HDX-MS core in School of Medicine, Emory University for their technical assistance in data collection and analysis. This study was supported in part by the Emory Integrated Genomics Core (EIGC), which is subsidized by the Emory University School of Medicine and is one of the Emory Integrated Core Facilities. The authors are grateful to the beamline staff at Argonne National Laboratory, South East Regional Collaborative Team, for support during remote collection of crystal diffraction data. This work was supported in part by the National Institutes of Health under the following awards: T32GM008602 (S.G.M.), F31DK111171 (S.G.M.), T32GM008367-27 (E.H.D.), R01DK095750 (E.A.O.), R01DK114213 (E.A.O., N.T.J., J.W.C). The work was also supported by an Emory Catalyst Award (E.A.O., N.T.J), and USDA ARS 3092-5-001-057 (D.D.M.). E.H.D was supported by the National Science Foundation Graduate Research Fellowship.

Figures

Figure 1

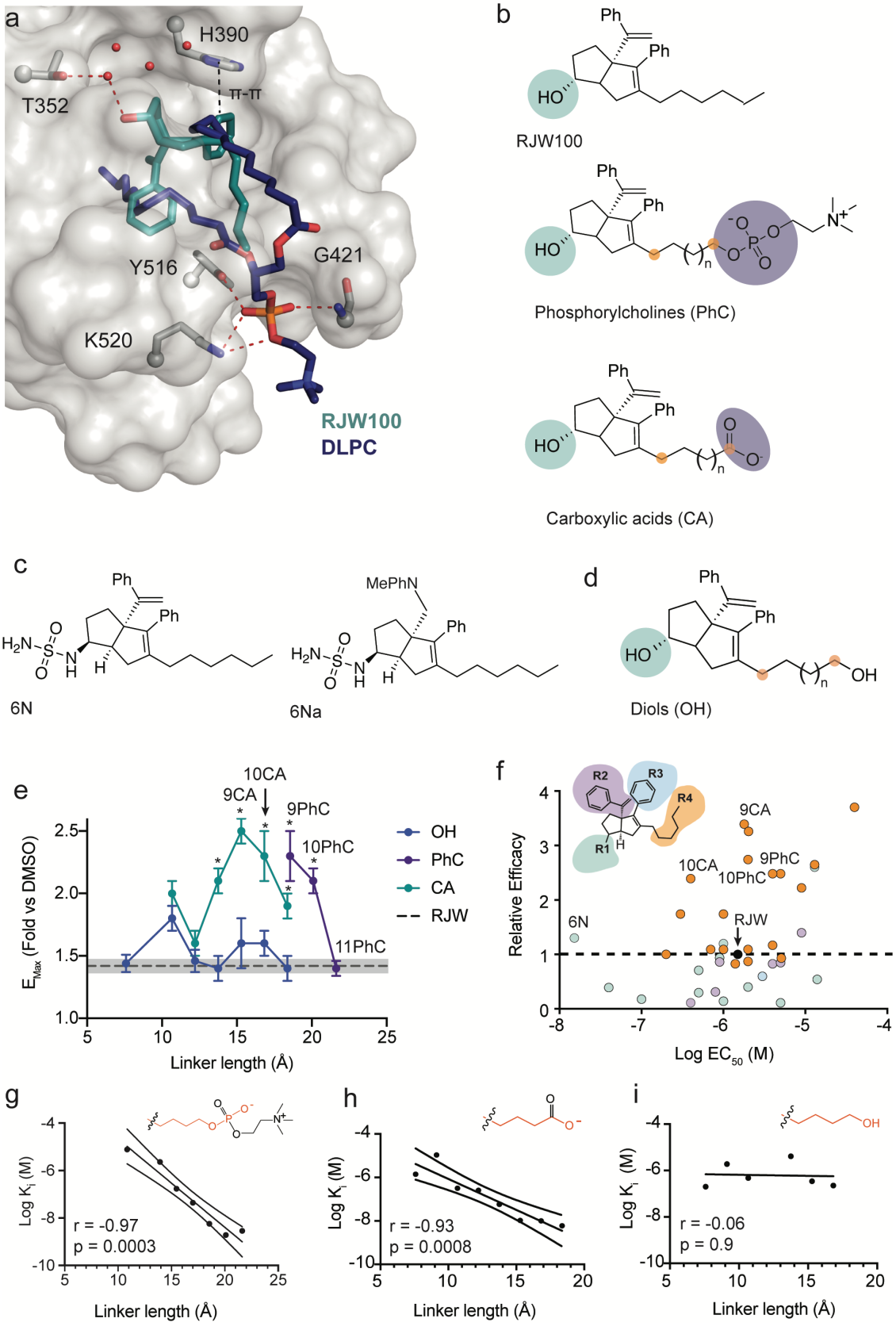
a
H390
T352
π-π
Y516
G421
K520
RJW100
DLPC
b
Ph
Ph
HO
RJW100
Phosphorylcholines (PhC)
Carboxylic acids (CA)
c
6N
6Na
MePhN
d
Diols (OH)
OH
e
10CA
9CA
9PhC
10PhC
11PhC
OH
PhC
CA
RJW
E_{Max} (Fold vs DMSO)
Linker length (Å)
f
R1
R2
R3
R4
9CA
10CA
9PhC
10PhC
6N
RJW
Relative Efficacy
Log EC_{50} (M)
g
Log K_i (M)
r = -0.97
p = 0.0003
Linker length (Å)
h
r = -0.93
p = 0.0008
i
r = -0.06
p = 0.9

Figure 1. Phospholipid mimetic design, binding affinity, and activity. (a) Cartoon representation of the LRH-1 ligand binding pocket (LBP) from PDB 5L11, showing the binding modes of the synthetic agonist, RJW100 (teal sticks). RJW100 contacts residues deep in the (LBP), including a water-mediated hydrogen bond with T352 and a π-π interaction with H390. The tail of RJW100 is positioned towards the mouth of the LBP, providing the opportunity to make phospholipid-like contacts with residues such as Y516, K520, G421, as shown here with superposition with DLPC (PDB 4DOS, dark blue sticks). (b) Agonist design strategy. Phosphorylcholines or carboxylic isosteres were conjugated to the RJW100 core via alkyl chain linkers of 4-11 carbons.[27] (c) Structures of agonists 6N[33] and 6Na,[30] which have unmodified tails but differ from RJW100 elsewhere on the scaffold. (d) Set of diols with alkyl chain linkers of 4-11 carbons synthesized for comparison with the PL mimics. (e) Plot of E_{max} values calculated from luciferase reporter assays as a function of linker length. Each point represents the mean ± SEM from 2-3 experiments conducted in triplicate. Compounds that did not activate sufficiently for an E_{max} to be calculated are omitted. *Dotted line* is the mean E_{max} of RJW100, with the grey shading indicating the SEM. *, $p < 0.05$ *versus* RJW100 by two-way ANOVA followed by Sidak's multiple comparisons test. (f) Plot comparing activity profiles of the PL-mimics to closely-related LRH-1 agonists. *Inset,* chemical structure of RJW100 indicating the sites of modification of compounds depicted in the plot. Relative efficacy refers to E_{max} relative to RJW100, calculated as described in the methods section. The PL-mimics have been modified at R_4 (orange dots), which has a greater effect on relative efficacy. Modifications to R_1 (teal dots)[33] affect EC_{50} values but have lesser effects on relative efficacy. (g-i) Binding affinity (K_i) plotted as a function of linker length. The CAs (*g*) and PhCs (*h*), but not diols (*i*) increase affinity for purified LRH-1 LBD in a tail-length dependent manner. *Lower insets in (g-i):* Pearson correlation coefficients (r) and p-values for each linear regression. *Upper insets in (g-i):* illustration of the portions of the molecules represented in the distances plotted on the x-axes.

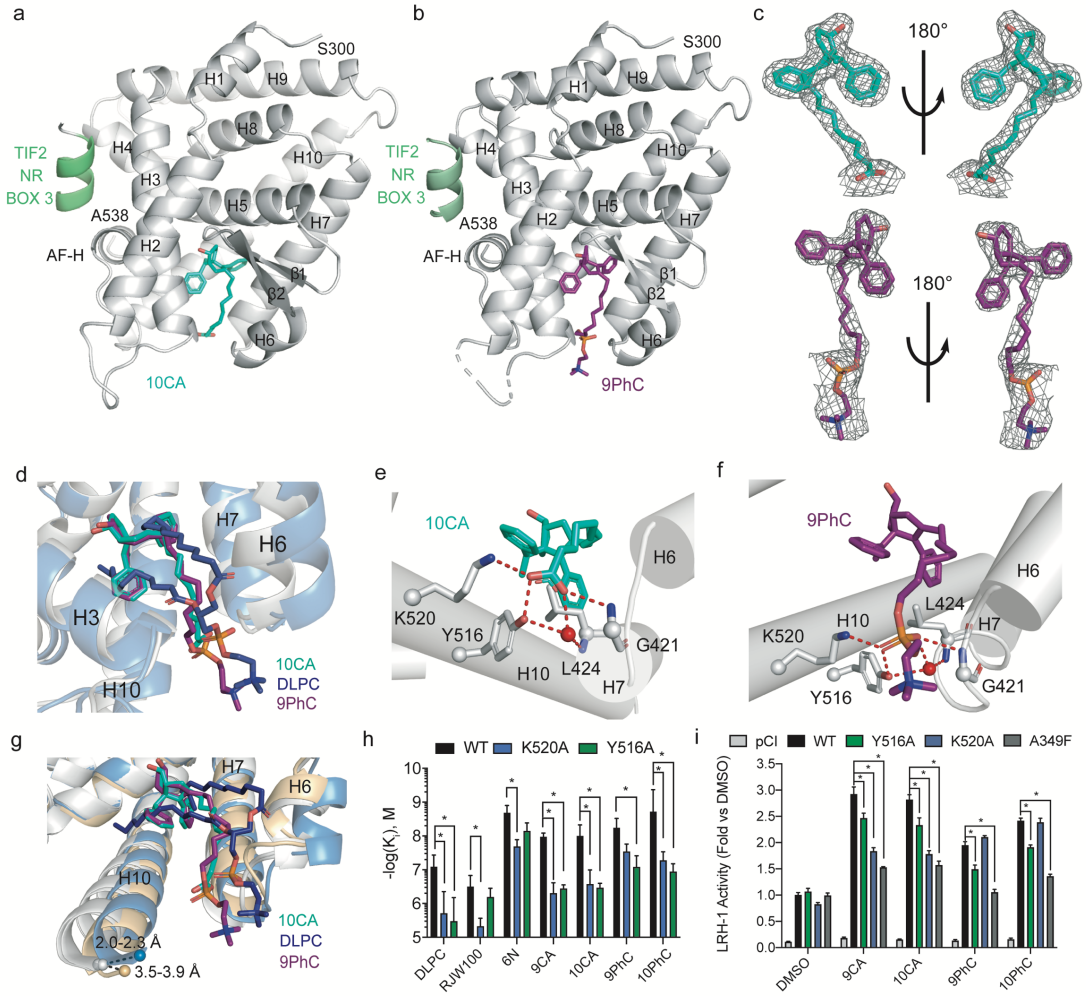

Figure 2. Phospholipid mimetics make PL-like interactions with LRH-1 ligand-binding pocket. Crystal structures of (*a*) 10CA (PDB: 7JYD) and (*b*) 9PhC (PDB: 7JYE) bound to the LRH-1 LBD and a fragment of the Tif2 coregulator. (c). Omit maps showing electron density surrounding 10CA (*top*) and 9PhC (*bottom*). Maps are F_o-F_c, contoured at 2σ. (d). Superposition of three ligands from LRH-1 structures: 10CA (cyan sticks), 9PhC (purple sticks), or DLPC (dark blue sticks, from PBD 4DOS[31]). The protein backbones of LRH-1 from the 10CA and DLPC structures are shown as grey and light blue cartoons, respectively. (e-f). Close-up view of the interactions made by the terminal polar groups of 10CA (*e)* and 9PhC (*f)* at the mouth of the LRH-1 binding pocket. Hydrogen bonds are shown with red dotted lines and a water molecule is shown as a red sphere. (g) Superposition of structures of LRH-1 in the apo state

(from PBD 4PLD, pale orange), LRH-1-DLPC (light blue protein backbone), LRH-1-10CA, and LRH-1-9PhC structures (the latter two both with grey protein backbones). DLPC displaces helix 6 relative to apo-LRH-1, whereas 10CA and 9PhC displace helix 10. (h) Effects of K520A or Y516A mutations on binding affinity. Each bar represents the mean ± the 95% CI from 2 experiments in quadruplicate. *, $p < 0.05$ by two-way ANOVA followed by Dunnett's test for multiple comparisons. (i) Luciferase reporter assays with full-length LRH-1 assess ability of longer tailed PL-mimetics to activate LRH-1 with K520A or Y516A mutations. The A349F mutation occludes the binding pocket and was used as a negative control. Cells were treated with 30 µM of each compound for 24 hours prior to measurement of luciferase signal. *, $p < 0.05$ *versus* WT LRH-1 treated with each agonist; (two-way ANOVA followed by Dunnett's test for multiple comparisons).

Figure 3

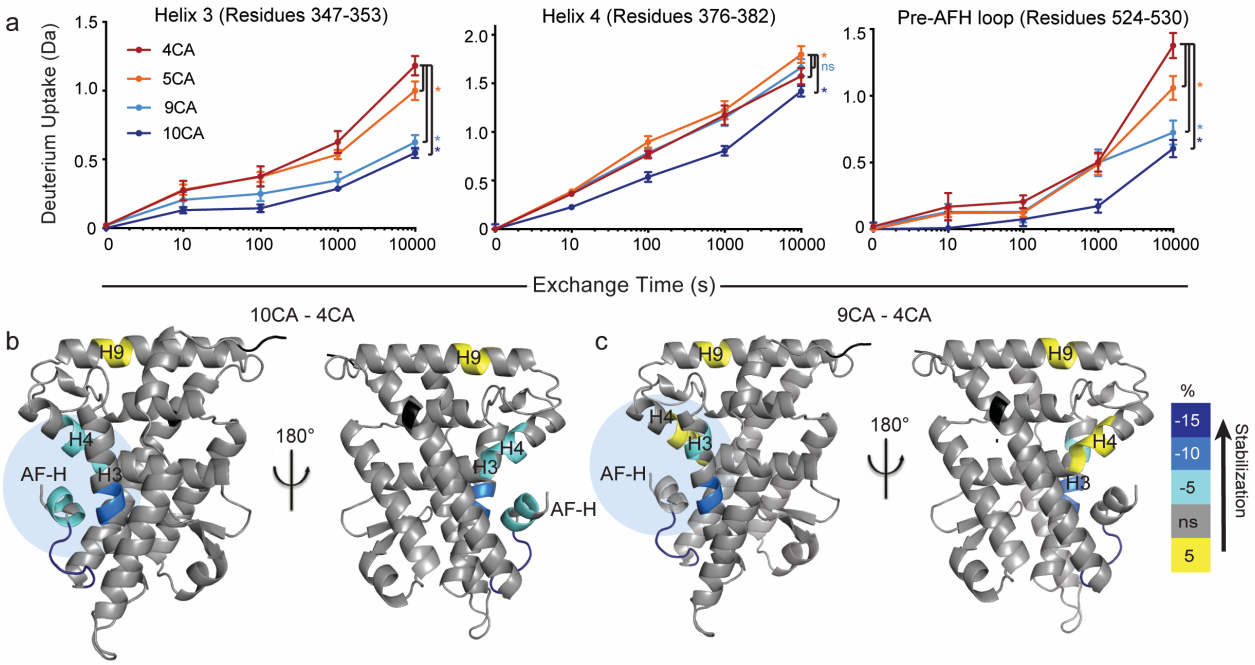

Figure 3. Longer-tailed PL mimetics stabilize the AFS in HDX-MS. (a) Deuterium uptake in regions within the activation function surface (AFS) of the LRH-1 LBD is more rapid and occurs to a greater extent for

4CA and 5CA compared to 9CA and 10CA. Each point represents the mean +/- SD for three replicates. Reduced deuterium exchange indicates greater stability. *, $p < 0.05$ (b-c). Differences in deuterium uptake (mean of all timepoints) are mapped onto the LRH-1 LBD for 10CA (*b*) and 9CA (*c*) *versus* 4C. The blue shaded circle indicates the location of the AFS. The scale bar indicates the colors associated with greater stabilization by 10CA or 9CA (teal and blue colors) or relative destabilization (yellow). Black indicates regions that were not mapped.

Figure 4

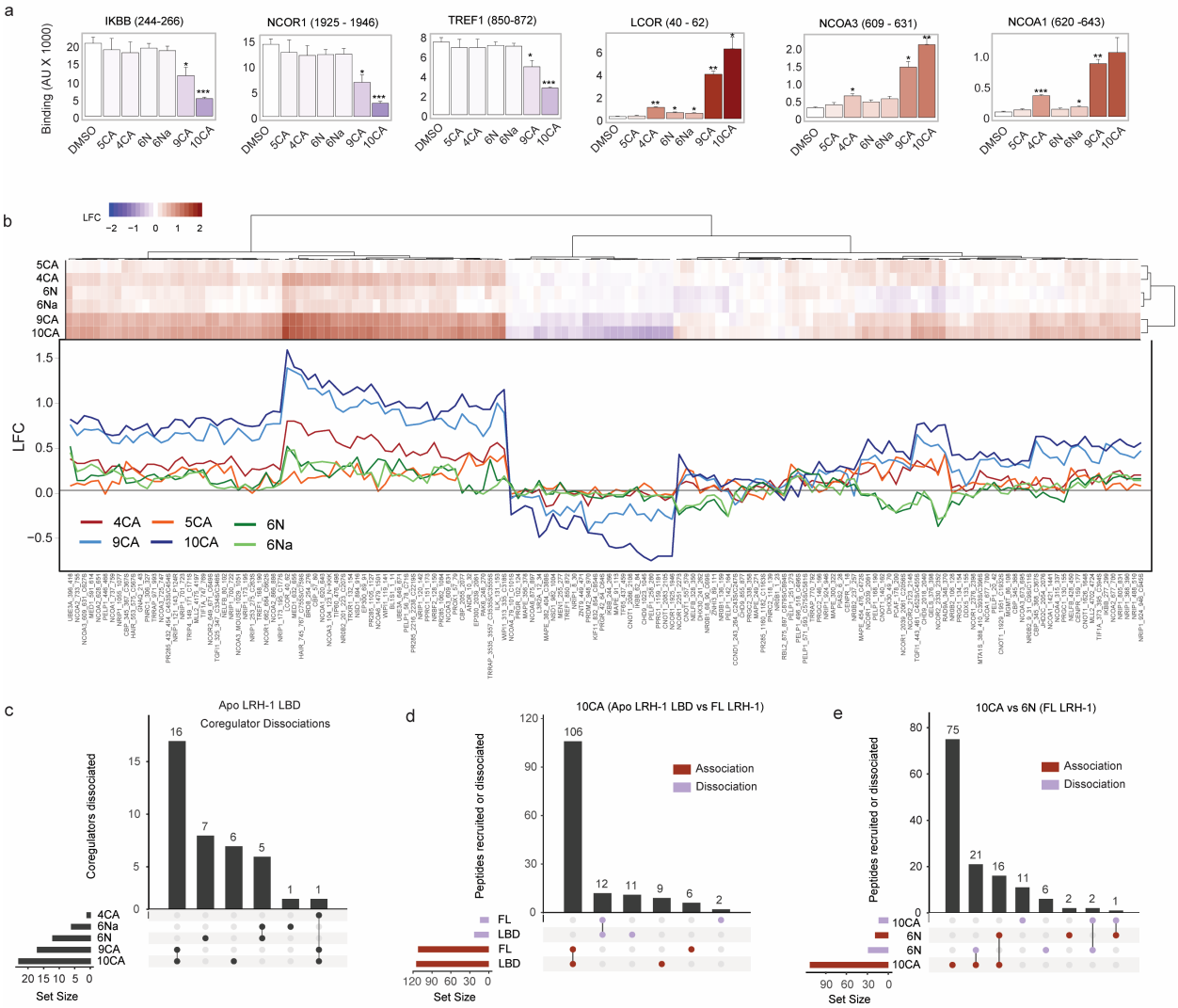

Figure 4. Coregulator recruitment profiling by MARCoNI. (a). Representative bar plots from the experiment, showing some of the most strongly affected coregulators by 9CA and 10CA. Each bar represents mean ± SEM from three replicates. Graph titles indicate the coregulator names, with the residue numbers of the coregulator peptide in parentheses. Statistically significant changes relative to DMSO control were identified by Student's t-test, post-hoc FDR, *, $p<0.05$, **, $p<0.01$ or ***, $p<0.001$. (b) Heat map and corresponding raw traces showing log fold change (LFC) in coregulator peptide binding relative to apo LRH-1-LBD. (c-e). Upset plots highlighting overlaps in coregulator binding events affected by at least 1.5-fold by various agonists or between experiments. Horizontal bars represent the number of events in each set, and vertical bars indicate numbers of events that overlap in between the groups that have filled-in circles below the vertical bars. For example, in panel *(c)*, the first vertical bar shows that a set of 16 coregulator peptides dissociate from LRH-1 in the presence of both 9CA and 10CA that are not affected by 6N and 6Na. (d) Upset plot comparing overlap in coregulator recruitment events by 10CA bound to full-length LRH-1 (FL) or LRH-1 ligand binding domain (LBD). Red bars indicate coregulators that associated to the 10CA-LRH-1 complex and purple bars indicate coregulator dissociation. (e) Upset plot highlighting an opposite recruitment pattern by compounds 10CA and 6N bound to FL-LRH-1.

Figure 5

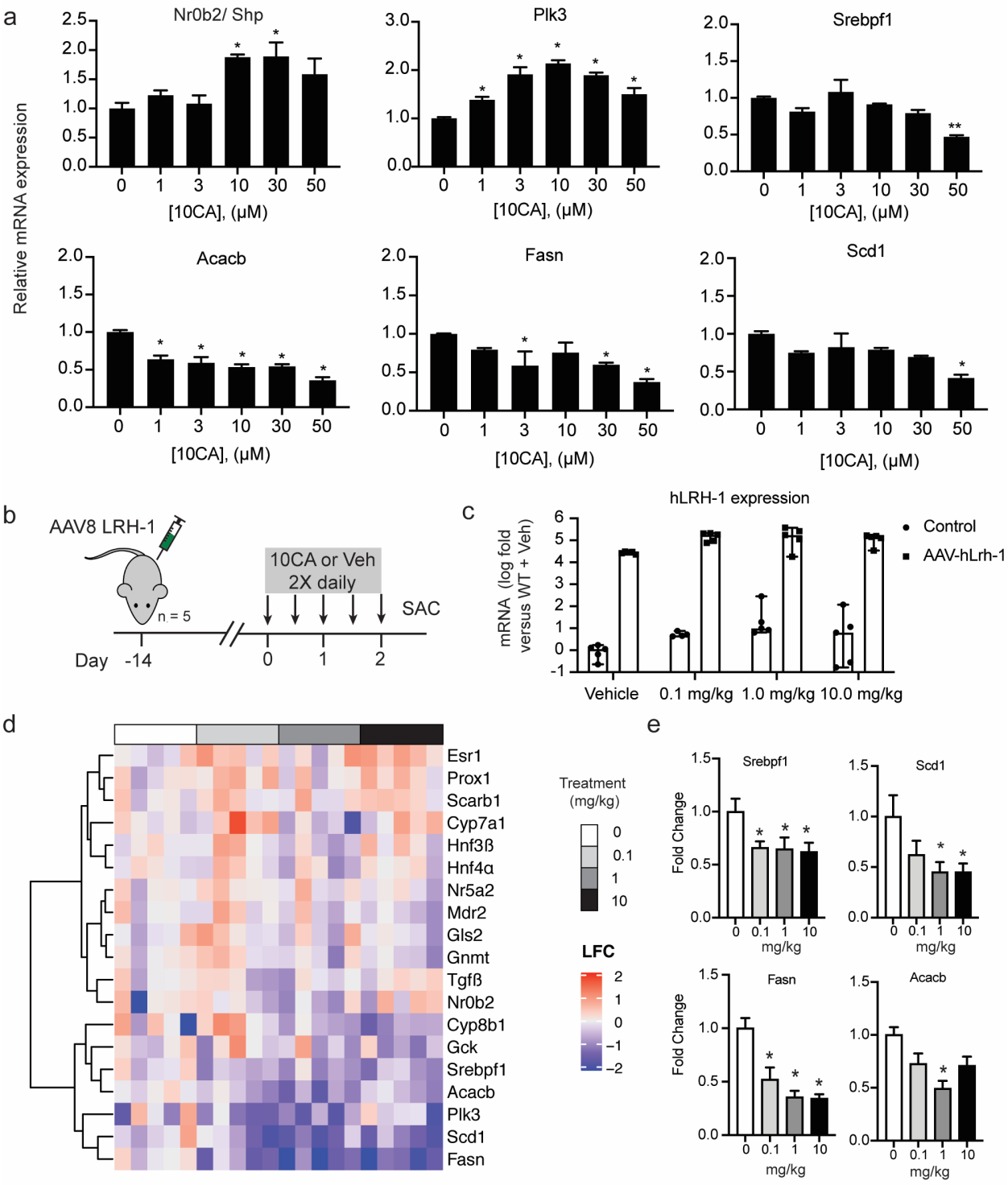
a
Nr0b2/ Shp
Plk3
Srebpf1
Acacb
Fasn
Scd1
Relative mRNA expression
[10CA], (μM)
b
AAV8 LRH-1
n = 5
10CA or Veh
2X daily
SAC
Day -14
0
1
2
c
hLRH-1 expression
mRNA (log fold versus WT + Veh)
Control
AAV-hLrh-1
Vehicle
0.1 mg/kg
1.0 mg/kg
10.0 mg/kg
d
Esr1
Prox1
Scarb1
Cyp7a1
Hnf3ß
Hnf4α
Nr5a2
Mdr2
Gls2
Gnmt
Tgfß
Nr0b2
Cyp8b1
Gck
Srebpf1
Acacb
Plk3
Scd1
Fasn
Treatment (mg/kg)
LFC
e
Fold Change
mg/kg

Figure 5. 10CA activates LRH-1 in hepatocytes and in the liver. (a) Treatment with 10CA dose-dependently upregulates expression of *SHP* and *PLK3* and downregulates LRH-1 targets involved in *de novo* lipogenesis in Huh7 hepatocytes (*SREBPF1*, *ACACB*, *FASN*, and *SCD1*). Cells were treated for 24 hours with doses of 10CA indicated in the x-axes. (b) Schematic of the experimental design for the mouse study. Mice were injected with AAV8-hLRH-1 intravenously to induce human LRH-1 expression, then after two weeks were treated with five doses of 10CA over three days. (c) Liver tissue from mice injected with hLRH-1-AAV8 was isolated and analyzed by qRT-PCR to measure levels of human LRH-1. Data are quantified relative to TBP. (d) Heatmap of Nanostring results in mice expressing hLRH-1 and treated with vehicle, 0.1, 1.0, or 10.0 mg/kg 10CA. (e) Individual bar graphs from Nanostring showing downregulation of lipogenic genes. *, $p < 0.05$.

Figure 6

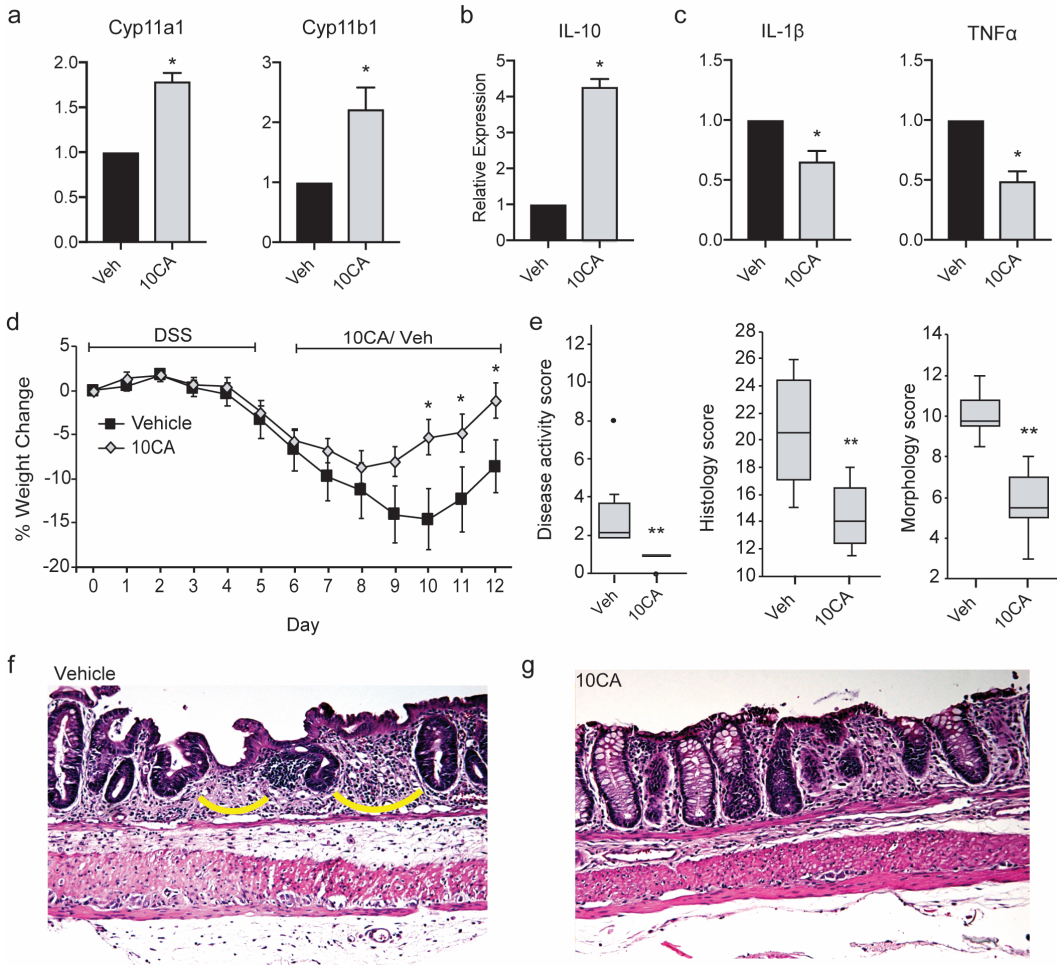

Figure 6. Efficacy of 10CA organoid and *in vivo* models of colitis. (a-c) qRT-PCR measuring gene expression changes in mouse enteroids (n = 3) expressing human LRH-1 and treated with either DMSO (Veh) or 10CA at 1 μM for 24 hours. 10CA induces expression of steroidogenic genes *Cyp11a1* and *Cyp11b1 (a),* increases expression of the anti-inflammatory cytokine IL-10 (*b*) and suppresses expression of the pro-inflammatory cytokines IL-1b and TNFα (*c*). (d) Plot of weight changes of mice in the DSS experiment. Each point represents the mean +/- SEM from 5 mice per group. Horizontal bars above the figure indicate periods of daily DSS or 10CA or Vehicle (Veh) administration. (e) Scores for disease activity scores, histology, and morphology were calculated as described in the methods section and Table S3. Boxes indicate the median and 1st and 3rd quartiles and whiskers indicate the range . (f-g)

Representative colon sections stained with H&E show reduced intestinal damage with 10CA treatment (*g*) compared to vehicle (*f*). Regions highlighted in yellow in panel (*f*) show examples of crypt loss.*, $p < 0.05$, **, $p < 0.01$ relative to vehicle-treated organoids or mice.

Authors will release the atomic coordinates and experimental data upon article publication. PDB IDs have been provided in figure legends and are as follows: LRH-1-10CA, 7JYD; LRH-1-9PhC, 7JYE.

References

1. van der Veen, J.N. et al. The critical role of phosphatidylcholine and phosphatidylethanolamine metabolism in health and disease. *Biochim Biophys Acta Biomembr* **1859,** 1558-1572 (2017).
2. Chaurio, R.A. et al. Phospholipids: key players in apoptosis and immune regulation. *Molecules* **14,** 4892-4914 (2009).
3. Dawaliby, R. et al. Allosteric regulation of G protein-coupled receptor activity by phospholipids. *Nat Chem Biol* **12,** 35-39 (2016).
4. Liu, S. et al. A diurnal serum lipid integrates hepatic lipogenesis and peripheral fatty acid use. *Nature* **502,** 550-554 (2013).
5. O'Donnell, V.B., Rossjohn, J. & Wakelam, M.J. Phospholipid signaling in innate immune cells. *J. Clin. Invest.* **128,** 2670-2679 (2018).
6. Wymann, M.P. & Scheiter, R. Lipid signalling in disease. *Nat Rev Mol Cell Biol* **9,** 162-176 (2008).
7. Li, Z. et al. The ratio of phosphatidylcholine to phosphatidylethanolamine influences membrane integrity and steatohepatitis. *Cell Metab.* **3,** 321-331 (2006).
8. Furse, S. & de Kroon, A.I. Phosphatidylcholine's functions beyond that of a membrane brick. *Mol Membr Biol* **32,** 117-119 (2015).
9. Walker, A.K. 1-Carbon Cycle Metabolites Methylate Their Way to Fatty Liver. *Trends Endocrinol Metab* **28,** 63-72 (2017).
10. Chakravarthy, M.V. et al. Identification of a physiologically relevant endogenous ligand for PPARalpha in liver. *Cell* **138,** 476-488 (2009).
11. Kang, H.W., Kanno, K., Scapa, E.F. & Cohen, D.E. Regulatory role for phosphatidylcholine transfer protein/StarD2 in the metabolic response to peroxisome proliferator activated receptor alpha (PPARα). *Biochimica et Biophysica Acta (BBA) - Molecular and Cell Biology of Lipids* **1801,** 496-502 (2010).
12. Musille, P.M. et al. Antidiabetic phospholipid-nuclear receptor complex reveals the mechanism for phospholipid-driven gene regulation. *Nat Struct Mol Biol* **19,** 532-537, S531-532 (2012).
13. Ortlund, E.A. et al. Modulation of human nuclear receptor LRH-1 activity by phospholipids and SHP. *Nat Struct Mol Biol* **12,** 357-363 (2005).
14. Musille, P.M., Kossmann, B.R., Kohn, J.A., Ivanov, I. & Ortlund, E.A. Unexpected Allosteric Network Contributes to LRH-1 Coregulator Selectivity. *J Biol Chem* (2015).
15. Sablin, E.P. et al. Structure of Liver Receptor Homolog-1 (NR5A2) with PIP hormone bound in the ligand binding pocket. *J Struct Biol* (2015).

16. Lee, J.M. et al. A nuclear-receptor-dependent phosphatidylcholine pathway with antidiabetic effects. *Nature* **474,** 506-510 (2011).
17. Mamrosh, J.L. et al. Nuclear receptor LRH-1/NR5A2 is required and targetable for liver endoplasmic reticulum stress resolution. *Elife* **3,** e01694 (2014).
18. Coste, A., Dubuquoy, L., Barnouin, R., Annicotte, J-S., Magnier, B. Notti, M., Corazza, N., Antal, M.C., Metzger, D., Desreumaux, P., Brunner, T., Auwerx, J., and Schoonjans, K. . LRH-1-mediated glucocorticoid synthesis in enterocytes protects against infalmmatory bowel disease. *Proc Natl Acad Sci U S A* **104,** 13098-13103.
19. Xu, P., Oosterveer, M.H., Stein, S., Demagny, H., Ryu, D., Moullan, N., Comment, A., Auwerx, J., Schoonjans, K. LRH-1-dependent programming of mitochondrial glutamine processing drives liver cancer. *Genes Dev* **30,** 1255-1260 (2016).
20. Nadolny, C. & Dong, X. Liver receptor homolog-1 (LRH-1): a potential therapeutic target for cancer. *Cancer Biol. Ther.* **16,** 997-1004 (2015).
21. Cobo-Vuilleumier, N. et al. LRH-1 agonism favours an immune-islet dialogue which protects against diabetes mellitus. *Nat. Commun.* **9,** 1488 (2018).
22. Bayrer, J.R. et al. LRH-1 Mitigates Intestinal Infammatory Disease by Maintaining Epithelial Homeostasis and Cell Survival. *bioRxiv* (2018).
23. Musille, P.M., Kossmann, B.R., Kohn, J.A., Ivanov, I. & Ortlund, E.A. Unexpected Allosteric Network Contributes to LRH-1 Coregulator Selectivity. *J. Biol. Chem.* **291,** 1411-1426 (2015).
24. Wagner, M. et al. Liver receptor homolog-1 is a critical determinant of methyl-pool metabolism. *Hepatology* **63,** 95-106 (2016).
25. Lin, C.J. & Wang, M.C. Microbial metabolites regulate host lipid metabolism through NR5A-Hedgehog signalling. *Nat Cell Biol* **19,** 550-557 (2017).
26. Choi, S. et al. Methyl-sensing nuclear receptor Liver Receptor Homolog-1 regulates mitochondrial function in mouse hepatocytes. *Hepatology* **71,** 1055-1069 (2019).
27. Flynn, A.R., Mays, S.G., Ortlund, E.A. & Jui, N.T. Development of Hybrid Phospholipid Mimics as Effective Agonists for Liver Receptor Homologue-1. *ACS Med. Chem. Lett.* **9,** 1051-1056 (2018).
28. Krylova, I.N. et al. Structural analyses reveal phosphatidyl inositols as ligands for the NR5 orphan receptors SF-1 and LRH-1. *Cell* **120,** 343-355 (2005).
29. Mays, S.G. et al. Development of the First Low Nanomolar Liver Receptor Homolog-1 Agonist through Structure-guided Design. *J Med Chem* (2019).
30. Cornelison, J.L. et al. Development of a new class of liver receptor homolog-1 (LRH-1) agonists by photoredox conjugate addition. *Bioorganic & Medicinal Chemistry Letters* **30**(2020).
31. Musille, P.M. et al. Antidiabetic phospholipid-nuclear receptor complex reveals the mechanism for phospholipid-driven gene regulation. *Nat. Struct. Mol. Biol.* **19,** 532-537, S531-532 (2012).
32. Mays, S.G. et al. Crystal Structures of the Nuclear Receptor, Liver Receptor Homolog 1, Bound to Synthetic Agonists. *J. Biol. Chem.* **291,** 25281-25291 (2016).
33. Koppen, A., Houtman, R., Pijenburg, D., Jeninga, E.H., Ruijtenbeek, R., Kalkhoven, E. Nuclear Receptor-Coregulator Interaction Profiling Identifies TRIP3 as a Novel Peroxisome Proliferator-activated Receptor. *Molecular and Cellular Proteomics***,** 2211-2226 (2009).
34. Na, S.-Y. et al. IkBb Interacts with the Retinoid X Receptor and Inhibits Retinoid-dependent Transactivation in Lipopolysaccharide-treated Cells. *J. Biol. Chem.* **273,** 3212-3215 (1998).
35. Mays, S.G. et al. Development of the first low nanomolar liver receptor homolog-1 agonist through structure-guided design. *J. Med. Chem.* **62,** 11022-11034 (2019).
36. Corneilson, J.L.C., M. L.; Johnson, A. M.; D'Agostino, E. H.; Melchers, D.; Patel, A. B.; Mays, S. G.; Houtman, R.; Ortlund, E. A.; Jui, N. T. Development of a new class of liver receptor homolog-1 (LRH-1) agonists by photoredox conjugate addition. *bioRxiv* (2020).

37. Lu, T. et al. Molecular Basis for Feedback Regulation of Bile Acid Synthesis by Nuclear Receptors. *Mol. Cell* **6,** 507-515 (2000).
38. Geiss, G.K., Bumgarner, R.E., Birditt, B., Dahl, T., Dowidar, N., Dunaway, D.L., Fell, H.P., Ferree, S., George, R.D., Grogan, T., James, J.J., Maysuria, M., Mitton, J.D., Oliveria, P., Osborn, J.L., Peng, T., Ratcliffe, A.L., Webster, P.J.,Davidson, E.H., Hood, L., Dimitrov, K. Direct multiplexed measurement of gene expression with color-coded probe pairs. *Nature Biotechnology* **26,** 317–325 (2008).
39. Ordás, I., Eckmann, L., Talamini, M., Baumgart, D.C. & Sandborn, W.J. Ulcerative colitis. *The Lancet* **380,** 1606-1619 (2012).
40. Coste, A. et al. LRH-1-mediated glucocorticoid synthesis in enterocytes protects against inflammatory bowel disease. *Proc Natl Acad Sci U S A* **104,** 13098-13103 (2007).
41. Mueller, M. et al. The nuclear receptor LRH-1 critically regulates extra-adrenal glucocorticoid synthesis in the intestine. *J. Exp. Med.* **203,** 2057-2062 (2006).
42. Bouguen, G. et al. Intestinal steroidogenesis controls PPARgamma expression in the colon and is impaired during ulcerative colitis. *Gut* **64,** 901-910 (2015).
43. Bayrer, J.R. et al. LRH-1 mitigates intestinal inflammatory disease by maintaining epithelial homeostasis and cell survival. *Nat. Commun.* **9,** 4055 (2018).
44. Basak, O. et al. Induced Quiescence of Lgr5+ Stem Cells in Intestinal Organoids Enables Differentiation of Hormone-Producing Enteroendocrine Cells. *Cell Stem Cell* **20,** 177-190 e174 (2017).
45. Chassaing, B., Aitken, J.D., Malleshappa, M. & Vijay-Kumar, M. Dextran sulfate sodium (DSS)-induced colitis in mice. *Curr Protoc Immunol* **104,** 15 25 11-15 25 14 (2014).
46. Chassaing, B., Aitken, J.D., Malleshappa, M. & Vijay-Kumar, M. Dextran sulfate sodium (DSS)-induced colitis in mice. *Curr Protoc Immunol* **104,** 1-14 (2014).
47. Treede, I. et al. Anti-inflammatory effects of phosphatidylcholine. *J. Biol. Chem.* **282,** 27155-27164 (2007).
48. Olson, A., Diebel, L.N. & Liberati, D.M. Exogenous phosphatidylcholine supplementation improves intestinal barrier defense against Clostridium difficile toxin. *J Trauma Acute Care Surg* **77,** 570-575; discussion 576 (2014).
49. Chen, M. et al. Phosphatidylcholine regulates NF-κB activation in attenuation of LPS-induced inflammation: evidence from in vitro study. *Animal Cells and Systems* **22,** 7-14 (2017).
50. Schneider, H., Braun, A., Fullekrug, J., Stremmel, W. & Ehehalt, R. Lipid based therapy for ulcerative colitis-modulation of intestinal mucus membrane phospholipids as a tool to influence inflammation. *Int J Mol Sci* **11,** 4149-4164 (2010).
51. MacDonald, J.I., Specher, H. Phospholipid Fatty Acid Remodeling in Mammalian Cells. *Biochim Biophys Acta, Lipids Lipid Metab* **1084,** 105-121 (1991).
52. Fernandez-Marcos, P.J., Auwerx, J. & Schoonjans, K. Emerging actions of the nuclear receptor LRH-1 in the gut. *Biochim Biophys Acta* **1812,** 947-955 (2011).
53. D'Agostino, E.H. et al. Development of a Versatile and Sensitive Direct Ligand Binding Assay for Human NR5A Nuclear Receptors. *ACS Med. Chem. Lett.* (2019).
54. Aarts, J.M. et al. Robust array-based coregulator binding assay predicting ERalpha-agonist potency and generating binding profiles reflecting ligand structure. *Chem Res Toxicol* **26,** 336-346 (2013).
55. Conway, J.R., Lex, A. & Gehlenborg, N. UpSetR: an R package for the visualization of intersecting sets and their properties. *Bioinformatics* **33,** 2938-2940 (2017).
56. Otwinowski, Z., Minor, W. Processing of X-Ray Diffraction Data Collected in Oscillation Mode. *Method. Enzymol.* **276,** 307-326 (1997).

57. Adams, P.D. et al. PHENIX: a comprehensive Python-based system for macromolecular structure solution. *Acta. Crystallogr. D Biol. Crystallogr.* **66,** 213-221 (2010).
58. Emsley, P. & Cowtan, K. Coot: model-building tools for molecular graphics. *Acta. Crystallogr. D Biol. Crystallogr.* **60,** 2126-2132 (2004).
59. Schrodinger, LLC. The PyMOL Molecular Graphics System, Version 1.3r1. (2010).
60. Laskowski, R.A. & Swindells, M.B. LigPlot+: multiple ligand-protein interaction diagrams for drug discovery. *J Chem Inf Model* **51,** 2778-2786 (2011).
61. Case, D.C., D.; Cheatham Iii, T.; Darden, T.; Duke, R.; Giese, T.; Gohlke, H.; Goetz, A.; Greene, D.; Homeyer, N.; Izadi, S.; Kovalenko, A.; Lee, T.; LeGrand, S.; Li, P.; Lin, C.; Liu, J.; Luchko, T.; Luo, R.; Mermelstein, D.; Merz, K. M.; Monard, G.; Nguyen, H.; Omelyan, I.; Onufriev, A.; Pan, F.; Qi, R.; Roe, D. R.; Roitberg, A.; Sagui, C.; Simmerling, C.; Botello-Smith, W.; Swails, J.; Walker, R.; Wang, J.; Wolf, R.; Wu, X.; Xiao, L.; York, D.; Kollman, P. AMBER 2017. *University of Californa, San Franscisco* (2017).
62. Maier, J.A.M., C.; Kasavajhala, K.; Wickstrom, L.; Hauser, K. E.; Simmerling, C. ff14SB: Improving the accuracy of protein side chain and backbone parameters from ff99SB. *Journal of chemical theory and computation* **11,** 3696-3713 (2015).
63. Wang, J.W., W.; Kollman, P. A.; Case, D. A. Antechamber: an accessory software package for molecular mechanical calculations. *J Am Chem Soc* **222,** U403 (2001).
64. Ryckaert, J.-P.C., G.; Berendsen, H. J. Numerical integration of the cartesian equations of motion of a system with constraints: molecular dynamics of n-alkanes. *Journal of Computational Physics* **23,** 327-341 (1977).
65. Roe, D.R.C.I., T. E. PTRAJ and CPPTRAJ: software for processing and analysis of molecular dynamics trajectory data. *Journal of chemical theory and computation* **9,** 3084-3095 (2013).